

# First Results on Dark Matter Annihilation in the Sun using the ANTARES Neutrino Telescope

S. Adrián-Martínez<sup>a</sup> I. Al Samarai<sup>b</sup> A. Albert<sup>c</sup> M. André<sup>d</sup> M. Anghinolfi<sup>e</sup> G. Anton<sup>f</sup> L. Anton<sup>f</sup> S. Anvar<sup>g</sup> M. Ardid<sup>a</sup> T. Astraatmadja<sup>h,1</sup> J.-J. Aubert<sup>b</sup> B. Baret<sup>i</sup> S. Basa<sup>j</sup> V. Bertin<sup>b</sup> S. Biagi<sup>k,l</sup> C. Bigongiari<sup>m</sup> C. Bogazzi<sup>h</sup> B. Bouhou<sup>i</sup> M.C. Bouwhuis<sup>h</sup> J. Brunner<sup>b</sup> J. Busto<sup>b</sup> A. Capone<sup>n,o</sup> C. Cârloganu<sup>p</sup> J. Carr<sup>b</sup> S. Cecchini<sup>k</sup> Z. Charif<sup>b</sup> Ph. Charvis<sup>q</sup> T. Chiarusi<sup>k</sup> M. Circella<sup>r</sup> F. Classen<sup>f</sup> R. Coniglione<sup>s</sup> L. Core<sup>b</sup> H. Costantini<sup>b</sup> P. Coyle<sup>b</sup> A. Creusot<sup>i</sup> C. Curtil<sup>b</sup> G. De Bonis<sup>n,o</sup> M.P. Decowski<sup>h</sup> I. Dekeyser<sup>t</sup> A. Deschamps<sup>q</sup> C. Distefano<sup>s</sup> C. Donzaud<sup>i,u</sup> D. Dornic<sup>b</sup> Q. Dorosti<sup>v</sup> D. Drouhin<sup>c</sup> A. Dumas<sup>p</sup> T. Eberl<sup>f</sup> U. Emanuele<sup>m</sup> A. Enzenhöfer<sup>f</sup> J.-P. Ernenwein<sup>b</sup> S. Escoffier<sup>b</sup> K. Fehn<sup>f</sup> P. Fermani<sup>n,o</sup> S. Ferry<sup>w</sup> V. Flaminio<sup>x,y</sup> F. Folger<sup>f</sup> U. Fritsch<sup>f</sup> J.-L. Fuda<sup>t</sup> S. Galatà<sup>b</sup> P. Gay<sup>p</sup> S. Geißelsöder<sup>f</sup> K. Geyer<sup>f</sup> G. Giacomelli<sup>k,l</sup> V. Giordano<sup>s</sup> A. Gleixner<sup>f</sup> J.P. Gómez-González<sup>m</sup> K. Graf<sup>f</sup> G. Guillard<sup>p</sup> G. Hallewell<sup>b</sup> M. Hamal<sup>z</sup> H. van Haren<sup>aa</sup> A.J. Heijboer<sup>h</sup> Y. Hello<sup>q</sup> J.J. Hernández-Rey<sup>m</sup> B. Herold<sup>f</sup> J. Höbl<sup>f</sup> C.C. Hsu<sup>h</sup> C. James<sup>f</sup> M. de Jong<sup>h,1</sup> M. Kadler<sup>ab</sup> O. Kalekin<sup>f</sup> A. Kappes<sup>f,2</sup> U. Katz<sup>f</sup> P. Kooijman<sup>h,ac,ad</sup> C. Kopper<sup>h,f</sup> A. Kouchner<sup>i</sup> I. Kreykenbohm<sup>ab</sup> V. Kulikovskiy<sup>ae,e</sup> R. Lahmann<sup>f</sup> G. Lambard<sup>m,3</sup> G. Larosa<sup>a</sup> D. Lattuada<sup>s</sup> D. Lefèvre<sup>t</sup> E. Leonora<sup>s,af</sup> D. Lo Presti<sup>s,af</sup> H. Loehner<sup>v</sup> S. Loucatos<sup>w</sup> F. Louis<sup>g</sup> S. Mangano<sup>m</sup> M. Marcelin<sup>j</sup> A. Margiotta<sup>k,l</sup> J.A. Martínez-Mora<sup>a</sup> S. Martini<sup>t</sup> T. Montaruli<sup>r,ah</sup> M. Morganti<sup>x,4</sup> H. Motz<sup>f</sup> C. Mueller<sup>ab</sup> M. Neff<sup>f</sup> E. Nezri<sup>j</sup> D. Palioselitis<sup>h</sup> G.E. Pāvāļš<sup>ai</sup> J. Petrovic<sup>h</sup> P. Piattelli<sup>s</sup> V. Popa<sup>ai</sup> T. Pradier<sup>aj</sup> C. Racca<sup>c</sup> C. Reed<sup>h</sup> G. Riccobene<sup>s</sup> R. Richter<sup>f</sup> C. Rivière<sup>b</sup> A. Robert<sup>t</sup> K. Roensch<sup>f</sup> A. Rostovtsev<sup>ak</sup> M. Rujoiu<sup>ai</sup> D. F. E. Samtleben<sup>h</sup>

<sup>1</sup>Also at University of Leiden, the Netherlands

<sup>2</sup>On leave of absence at the Humboldt-Universität zu Berlin

<sup>3</sup>Corresponding author, Email address: lambard@ific.uv.es

<sup>4</sup>Also at Accademia Navale de Livorno, Livorno, Italy

**A. Sánchez-Losa<sup>m</sup> P. Sapienza<sup>s</sup> J. Schmid<sup>f</sup> J. Schnabel<sup>f</sup> S. Schulte<sup>h</sup> F. Schüssler<sup>w</sup> T. Seitz<sup>f</sup> R. Shanidze<sup>f</sup> F. Simeone<sup>n,o</sup> A. Spies<sup>f</sup> M. Spurio<sup>k,l</sup> J.J.M. Steijger<sup>h</sup> Th. Stolarczyk<sup>w</sup> M. Taiuti<sup>e,al</sup> C. Tamburini<sup>t</sup> A. Trovato<sup>a,f</sup> B. Vallage<sup>w</sup> C. Vallée<sup>b</sup> V. Van Elewyck<sup>i</sup> P. Vernin<sup>w</sup> E. Visser<sup>h</sup> S. Wagner<sup>f</sup> G. Wijnker<sup>h</sup> J. Wilms<sup>ab</sup> E. de Wolf<sup>h,ad</sup> K. Yatkin<sup>b</sup> H. Yepes<sup>m</sup> D. Zaborov<sup>ak</sup> J.D. Zornoza<sup>m</sup> J. Zúñiga<sup>m</sup>**

<sup>a</sup>Institut d'Investigació per a la Gestió Integrada de les Zones Costaneres (IGIC) - Universitat Politècnica de València. C/ Paranimf 1 , 46730 Gandia, Spain.

<sup>b</sup>CPPM, Aix-Marseille Université, CNRS/IN2P3, Marseille, France

<sup>c</sup>GRPHE - Institut universitaire de technologie de Colmar, 34 rue du Grillenbreit BP 50568 - 68008 Colmar, France

<sup>d</sup>Technical University of Catalonia, Laboratory of Applied Bioacoustics, Rambla Exposició,08800 Vilanova i la Geltrú,Barcelona, Spain

<sup>e</sup>INFN - Sezione di Genova, Via Dodecaneso 33, 16146 Genova, Italy

<sup>f</sup>Friedrich-Alexander-Universität Erlangen-Nürnberg, Erlangen Centre for Astroparticle Physics, Erwin-Rommel-Str. 1, 91058 Erlangen, Germany

<sup>g</sup>Direction des Sciences de la Matière - Institut de recherche sur les lois fondamentales de l'Univers - Service d'Electronique des Détecteurs et d'Informatique, CEA Saclay, 91191 Gif-sur-Yvette Cedex, France

<sup>h</sup>Nikhef, Science Park, Amsterdam, The Netherlands

<sup>i</sup>APC, Université Paris Diderot, CNRS/IN2P3, CEA/IRFU, Observatoire de Paris, Sorbonne Paris Cité, 75205 Paris, France

<sup>j</sup>LAM - Laboratoire d'Astrophysique de Marseille, Pôle de l'Étoile Site de Château-Gombert, rue Frédéric Joliot-Curie 38, 13388 Marseille Cedex 13, France

<sup>k</sup>INFN - Sezione di Bologna, Viale Berti-Pichat 6/2, 40127 Bologna, Italy

<sup>l</sup>Dipartimento di Fisica dell'Università, Viale Berti Pichat 6/2, 40127 Bologna, Italy

<sup>m</sup>IFIC - Instituto de Física Corpuscular, Edificios Investigación de Paterna, CSIC - Universitat de València, Apdo. de Correos 22085, 46071 Valencia, Spain

<sup>n</sup>INFN -Sezione di Roma, P.le Aldo Moro 2, 00185 Roma, Italy

<sup>o</sup>Dipartimento di Fisica dell'Università La Sapienza, P.le Aldo Moro 2, 00185 Roma, Italy

<sup>p</sup>Clermont Université, Université Blaise Pascal, CNRS/IN2P3, Laboratoire de Physique Corpusculaire, BP 10448, 63000 Clermont-Ferrand, France

<sup>q</sup>Géoazur - Université de Nice Sophia-Antipolis, CNRS/INSU, IRD, Observatoire de la Côte d'Azur and Université Pierre et Marie Curie, BP 48, 06235 Villefranche-sur-mer, France

<sup>r</sup>INFN - Sezione di Bari, Via E. Orabona 4, 70126 Bari, Italy

<sup>s</sup>INFN - Laboratori Nazionali del Sud (LNS), Via S. Sofia 62, 95123 Catania, Italy

<sup>t</sup>Mediterranean Institute of Oceanography (MIO), Aix-Marseille University, 13288, Marseille, Cedex 9, France; Université du Sud Toulon-Var, 83957, La Garde Cedex, France CNRS-INSU/IRD UM 110

<sup>u</sup>Univ Paris-Sud , 91405 Orsay Cedex, France

<sup>v</sup>Kernfysisch Versneller Instituut (KVI), University of Groningen, Zernikelaan 25, 9747 AA Groningen, The Netherlands

<sup>w</sup>Direction des Sciences de la Matière - Institut de recherche sur les lois fondamentales de l'Univers - Service de Physique des Particules, CEA Saclay, 91191 Gif-sur-Yvette Cedex, France

<sup>x</sup>INFN - Sezione di Pisa, Largo B. Pontecorvo 3, 56127 Pisa, Italy

<sup>y</sup>Dipartimento di Fisica dell'Università, Largo B. Pontecorvo 3, 56127 Pisa, Italy

<sup>z</sup>University Mohammed I, Laboratory of Physics of Matter and Radiations, B.P.717, Oujda 6000, Morocco

<sup>aa</sup>Royal Netherlands Institute for Sea Research (NIOZ), Landsdiep 4,1797 SZ 't Horntje (Texel), The Netherlands

<sup>ab</sup>Dr. Remeis-Sternwarte and ECAP, Universität Erlangen-Nürnberg, Sternwartstr. 7, 96049 Bamberg, Germany

<sup>ac</sup>Universiteit Utrecht, Faculteit Betawetenschappen, Princetonplein 5, 3584 CC Utrecht, The Netherlands

<sup>ad</sup>Universiteit van Amsterdam, Instituut voor Hoge-Energie Fysica, Science Park 105, 1098 XG Amsterdam, The Netherlands

<sup>ae</sup>Moscow State University,Skobeltsyn Institute of Nuclear Physics,Leninskie gory, 119991 Moscow, Russia

<sup>af</sup>INFN - Sezione di Catania, Viale Andrea Doria 6, 95125 Catania, Italy

<sup>ag</sup>Dipartimento di Fisica ed Astronomia dell'Università, Viale Andrea Doria 6, 95125 Catania, Italy

<sup>ah</sup>Département de Physique Nucléaire et Corpusculaire, Université de Genève, 1211, Geneva, Switzerland

<sup>ai</sup>Institute for Space Sciences, R-77125 Bucharest, Măgurele, Romania

<sup>aj</sup>IPHC-Institut Pluridisciplinaire Hubert Curien - Université de Strasbourg et CNRS/IN2P3 23 rue du Loess, BP 28, 67037 Strasbourg Cedex 2, France

<sup>ak</sup>ITEP - Institute for Theoretical and Experimental Physics, B. Cheremushkinskaya 25, 117218 Moscow, Russia

<sup>al</sup>Dipartimento di Fisica dell'Università, Via Dodecaneso 33, 16146 Genova, Italy

**Abstract.** A search for high-energy neutrinos coming from the direction of the Sun has been performed using the data recorded by the ANTARES neutrino telescope during 2007 and 2008. The neutrino selection criteria have been chosen to maximize the selection of possible signals produced by the self-annihilation of weakly interacting massive particles accumulated in the centre of the Sun with respect to the atmospheric background. After data unblinding, the number of neutrinos observed towards the Sun was found to be compatible with background expectations. The 90% CL upper limits in terms of spin-dependent and spin-independent WIMP-proton cross-sections are derived and compared to predictions of two supersymmetric models, CMSSM and MSSM-7. The ANTARES limits are comparable with those obtained by other neutrino observatories and are more stringent than those obtained by direct search experiments for the spin-dependent WIMP-proton cross-section in the case of hard self-annihilation channels ( $W^+W^-$ ,  $\tau^+\tau^-$ ).

**Keywords:** dark matter, neutrino telescope, indirect detection, supersymmetry.

---

## Contents

<b>1</b>	<b>Introduction</b>	<b>1</b>
<b>2</b>	<b>The ANTARES Neutrino Telescope</b>	<b>2</b>
<b>3</b>	<b>Signal and background simulation</b>	<b>3</b>
<b>4</b>	<b>Optimisation of the event selection criteria</b>	<b>6</b>
<b>5</b>	<b>Results and discussion</b>	<b>8</b>

---

## 1 Introduction

There is compelling evidence from cosmology and astrophysics that about 83 % of the matter in the Universe is non-baryonic, non-relativistic and does not interact electromagnetically — the so-called dark matter [1, 2]. Much of this evidence comes from the internal dynamics of galaxy clusters [3], the rotation curves of galaxies [4], the observations from weak lensing (1E0657 – 558) [5], but also from the Cosmic Microwave Background (CMB), the large scale structure formation and type Ia supernovae. The determination of the relic density of cold dark matter (CDM) in the Universe is  $\Omega_{\text{CDM}}h^2 = 0.1120 \pm 0.0056$  using observations of the CMB [6]. A popular hypothesis is that dark matter is made of Weakly Interacting Massive Particles (WIMPs) that are embedded in the visible baryonic part of galaxies and surround them in the form of a halo. There are a variety of candidates for WIMPs, among which those provided by theories based on supersymmetry (SUSY) attract a great deal of interest. In some classes of the minimal supersymmetric extension of the Standard Model (MSSM), the lightest supersymmetric particle (LSP) is stable thanks to the conservation of R-parity that forbids its decay to standard particles. Consequently, the LSP can only annihilate in pairs, making it a good WIMP candidate for dark matter [7, 8]. In these models, high-energy neutrinos are produced from the decay of the LSPs’ self-annihilation products. Two simplified versions of the MSSM model are considered in this paper, the constrained MSSM (CMSSM) [9] and the low-energy phenomenological model MSSM-7 [10]. Both have a neutralino as the LSP.

The search for WIMPs can be performed either directly by recording the recoil energy of nuclei when WIMPs scatter off them in suitable detectors, or indirectly. The indirect approach, which is adopted here, exploits a radiation signature (gamma-ray, synchrotron, positron, anti-proton or neutrino flux) produced by the self-annihilations of WIMPs accumulated in astrophysical objects such as the galactic halo, the Sun or the Earth [11].

For the case of the Sun, dealt with in the paper, WIMPs can scatter elastically and become gravitationally trapped in its core. Here, the self-annihilation rate reaches a maximum when in equilibrium with the capture rate over the age of the Solar System [12]. The WIMPs self-annihilate to Standard Model (SM) particles whose decay or hadronisation give rise to the production of energetic neutrinos which can escape from the Sun and be detected by neutrino telescopes on the Earth. The accumulation of WIMPs in the Sun must have taken place during a large period of time and therefore a very wide region in the Galaxy must have contributed, thereby reducing the dependence of the overall capture on the detailed sub-structures of the dark matter halo distribution. Moreover, high-energy neutrinos (above

several GeV) coming from the Sun could not be explained by other known astrophysical processes.

In this paper an indirect search for dark matter by looking for high-energy neutrinos coming from the Sun, using the 2007-2008 data recorded by the ANTARES neutrino telescope, is reported. The layout of the paper is as follows. In Section 2, the main features of the ANTARES neutrino telescope and the reconstruction algorithm used in this work are described. In Section 3, the Monte Carlo simulation of the WIMP signal, the background expected from atmospheric muons and neutrinos, and the grid scan performed to explore the parameter space of the CMSSM and MSSM-7 models are reported. In Section 4, the method used to optimise the selection of the neutrino events is described. Finally, the results obtained are discussed in Section 5, where limits on the neutrino flux are derived from the absence of a signal coming from the Sun's direction. The corresponding limits on the spin-dependent and the spin-independent WIMP-proton cross-sections are obtained and compared to the predictions of the CMSSM and MSSM-7 theoretical models.

## 2 The ANTARES Neutrino Telescope

ANTARES is the first undersea neutrino telescope and the largest of its kind in the Northern Hemisphere [13]. It is located between 2475 m (seabed) and 2025 m below the Mediterranean Sea level, 40 km offshore from Toulon (France) at  $42^{\circ}48'$  N and  $6^{\circ}10'$  E. The telescope consists of 12 detection lines with 25 storeys each. A standard storey includes three optical modules (OMs) [14] each housing a 10-inch photomultiplier [15] and a local control module that contains the electronics [16, 17]. The OMs are orientated  $45^{\circ}$  downwards in order to optimise their acceptance to upgoing light and to avoid the effect of sedimentation and biofouling [18]. The length of a line is 450 m and the horizontal distance between neighbouring lines is 60-75 m. In one of the lines, the upper storeys are dedicated to a test system for acoustic neutrino detection [19]. Similar acoustic devices are also installed in an additional line that contains instrumentation aimed to measure environmental parameters [20]. The location of the active components of the lines is known better than 10 cm by a combination of tiltmeters and compasses in each storey and a series of acoustic transceivers (emitters and receivers) in certain storeys along the line and surrounding the telescope [21]. A common time reference is maintained in the full detector by means of a 25 MHz clock signal broadcast from shore. The time offsets of the individual optical modules are determined in dedicated calibration facilities onshore and regularly monitored in situ by means of optical beacons distributed at various points of the apparatus which emit short light pulses through the water [22]. This allows to reach a sub-nanosecond accuracy on the relative timing [23]. Additional information on the detector can be found in Reference [13].

A high-energy muon (anti-)neutrino interacts in the matter below the detector producing a relativistic muon that can travel hundreds of metres and cross the detector or pass nearby. This muon induces Cherenkov light when travelling through the water, which is detected by the OMs. From the time and position information of the photons provided by the OMs, the direction of the muon is reconstructed and is well correlated to the neutrino direction.

Data taking started with the first 5 lines of the detector installed in 2007. The full detector was completed in May 2008 and has been operating continuously ever since, except for some periods in which repair and maintenance operations have taken place. Other physics results using this data-taking period can be found elsewhere [24-26].

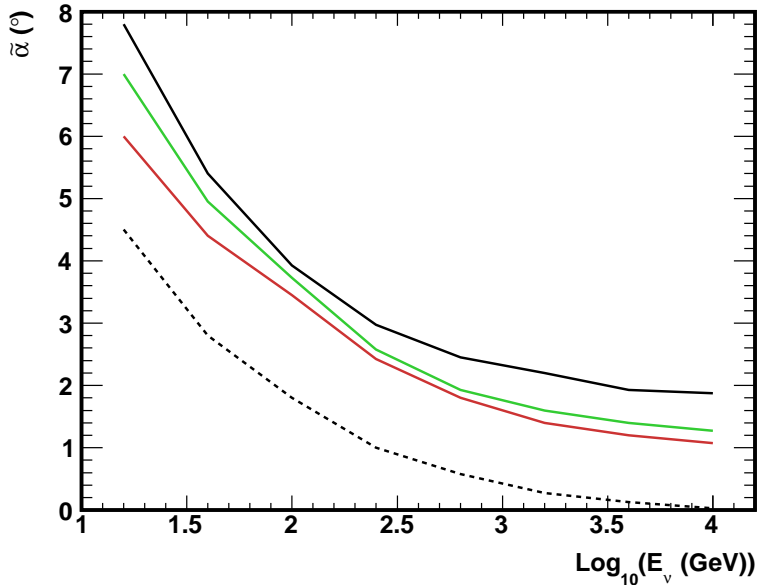


**Figure 1.** Median angular error,  $\tilde{\alpha}$  ( $^{\circ}$ ), on the upgoing neutrino track (solid lines) in the energy range of interest  $E_{\nu} \leq 10$  TeV, for 5 (black), 9 (green), and 12 (red) line configuration of the detector (10 and 12 line angular resolution are identical). The black dashed line shows only the kinematic counterpart at the neutrino-muon vertex of interaction.

A muon track is reconstructed from the position and time of the hits of the Cherenkov photons in the OMs. The reconstruction algorithm [27] is based on the minimisation of a  $\chi^2$ -like quality parameter,  $Q$ , which uses the differences between the expected and measured times of the detected photons plus a correction term that takes into account the effect of light absorption:

$$Q = \sum_{i=1}^{N_{\text{hit}}} \left[ \frac{(t_{\gamma} - t_i)^2}{\sigma_i^2} + \frac{A(a_i)D(d_{\gamma})}{\langle a \rangle d_0} \right], \quad (2.1)$$

where  $t_{\gamma}$  and  $t_i$  are respectively the expected and recorded arrival time of the photons from the track, and  $\sigma_i^2$  is the timing variance. The second term takes into account the accumulation of high charges in storeys close to the track. This term uses the measured hit charge,  $a_i$ , the average hit charge calculated from all hits which have been selected for the fit,  $\langle a \rangle$ , and the calculated photon travel distance,  $d_{\gamma}$ , together with a normalisation value,  $d_0$ . The functions  $A(a_i)$  and  $D(d_{\gamma})$  are discussed at length in Reference [27].

Depending on the configuration of the detector (see Section 4) and the muon (anti-) neutrino energy, this algorithm yields an angular resolution on the upgoing neutrino direction between 1 and 7.8 degrees as illustrated by the Figure 1.

### 3 Signal and background simulation

The flux of neutrinos as a function of their energy arriving at the Earth's surface from the Sun's core is computed using the software package WimpSim [28] without theoretical assump-

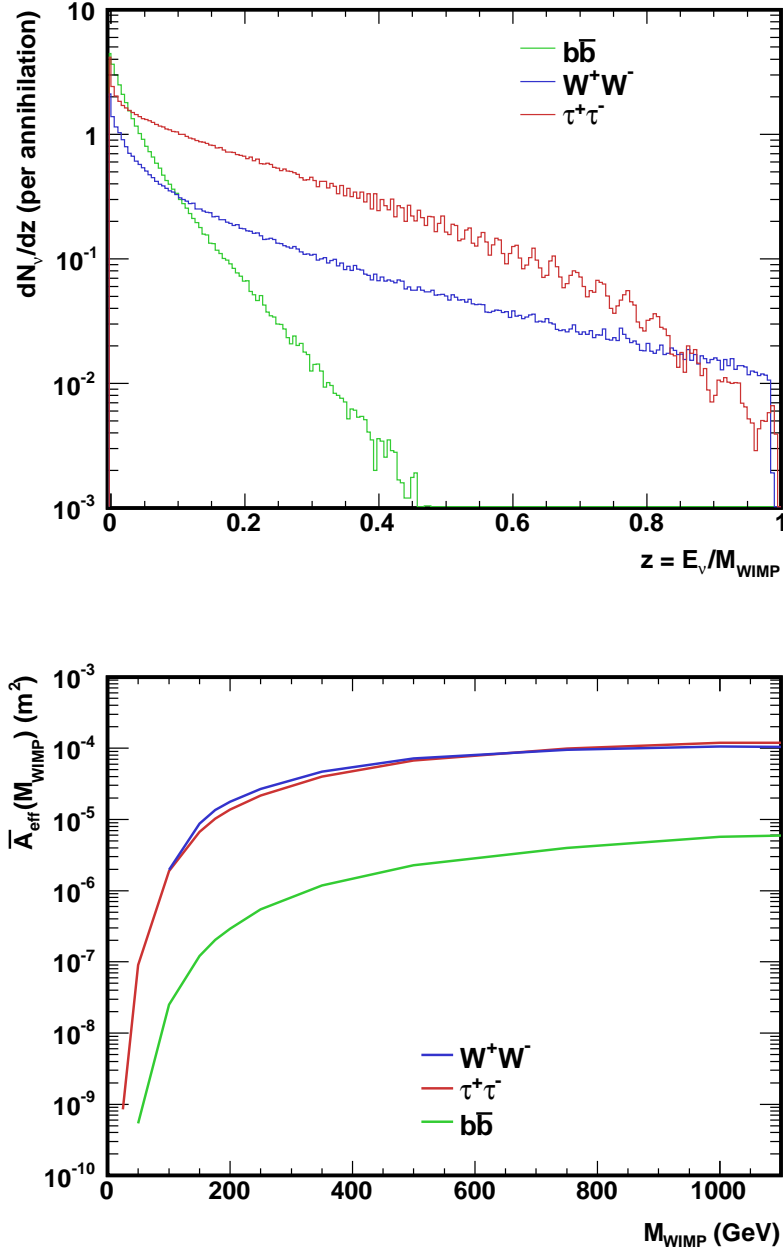


**Figure 2.** **Top:** Distribution of the number of muon neutrinos at the surface of the Earth as a function of their energy normalised to the WIMP mass for the channels:  $b\bar{b}$  (green),  $W^+W^-$  (blue),  $\tau^+\tau^-$  (red) for a WIMP mass  $M_{WIMP} = 350$  GeV, as an example. **Bottom:** Examples of the averaged effective area  $\bar{A}_{eff}(M_{WIMP})$  for the signal of WIMP self-annihilation inside the Sun,  $b\bar{b}$  (green),  $W^+W^-$  (blue) and  $\tau^+\tau^-$  (red) channels. The detector is in a 12 line configuration and  $(Q_{cut}, \Psi_{cut}) = (1.4, 3^\circ)$ .

tions concerning the dark matter model. The neutrinos resulting from the self-annihilation channels were simulated for 16 different WIMP masses in the range from 50 GeV to 10 TeV.

Three main self-annihilation channels are chosen as benchmarks for the lightest neu-

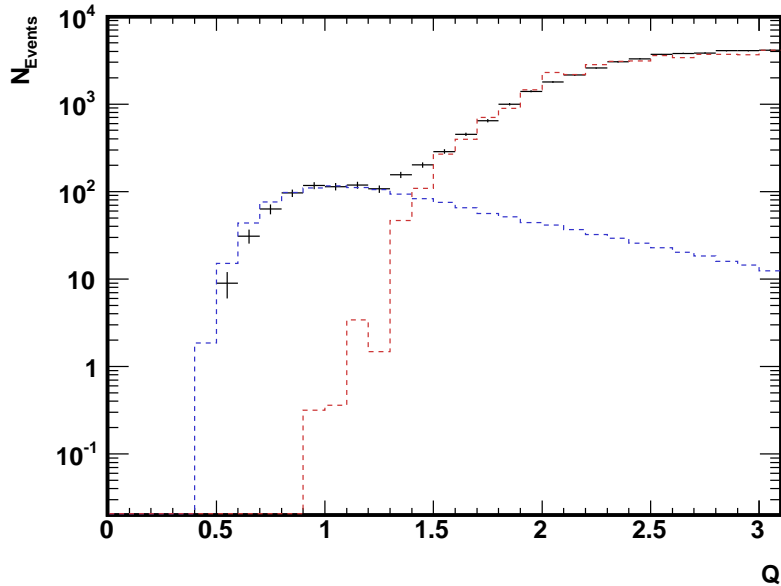


**Figure 3.** Distribution of the track fit quality parameter,  $Q$ . The blue and red dashed lines are, respectively, the expectations for atmospheric neutrino and muon events according to simulation and the black crosses are the 2007-2008 data.

tralino,  $\tilde{\chi}_1^0$ , namely: a soft neutrino channel,  $\tilde{\chi}_1^0\tilde{\chi}_1^0 \rightarrow b\bar{b}$ , and two hard neutrino channels,  $\tilde{\chi}_1^0\tilde{\chi}_1^0 \rightarrow W^+W^-$  and  $\tilde{\chi}_1^0\tilde{\chi}_1^0 \rightarrow \tau^+\tau^-$ . As the region in the SUSY parameter space determines which of these three channels is dominant, a 100% branching ratio is assumed for all of them in order to explore the widest theoretical parameter space [29–33]. The distribution of the number of muon neutrinos,  $dN_\nu/dz$ , arriving at the Earth per pair of WIMPs self-annihilating in the Sun’s core as a function of the energy ratio,  $z = E_\nu/M_{\text{WIMP}}$ , is shown in Figure 2 (top) for the channels  $b\bar{b}$ ,  $W^+W^-$  and  $\tau^+\tau^-$  (equivalent spectra are determined for muon anti-neutrinos). In this simulation, oscillations among the three neutrino flavours (both in the Sun and during their flight to Earth) are taken into account, as well as  $\nu$  absorption and  $\tau$  lepton regeneration in the Sun’s medium.

The main backgrounds for cosmic neutrinos in a neutrino telescope are atmospheric muons and neutrinos, both produced in the interactions of cosmic rays with the Earth’s atmosphere. Downgoing atmospheric muons dominate the trigger rate, which ranges from 3 to 10 Hz depending on the exact trigger conditions. They are simulated using Corsika [34]. Upgoing atmospheric neutrinos, which are recorded at a rate of  $\sim 50 \mu\text{Hz}$  (about four per day), are simulated according to the parameterisation of the atmospheric  $\nu_\mu$  flux from Reference [35] in the energy range from 10 GeV to 10 PeV. The Cherenkov light produced in the vicinity of the detector is propagated taking into account light absorption and scattering in sea water [36]. The angular acceptance, quantum efficiency and other characteristics of the PMTs are taken from Reference [14] and the overall geometry corresponds to the different layouts of the ANTARES detector during each data-taking period.

A source of background specific to this search is due to the interaction of cosmic rays



with the Sun’s corona. The interaction products may give rise to neutrinos in their decay. Using a simple parameterisation of the estimated  $\nu_\mu$  flux from Reference [37] in the energy range from 10 GeV to 10 PeV, this background is found to amount to less than 0.4 % of the total atmospheric background in the direction of the Sun and therefore neglected.

To reduce the background from atmospheric muons, only upgoing events occurring during a period in which the Sun was below the horizon are kept. The residual contamination from misreconstructed downgoing muons is reduced using the quality parameter from Equation 2.1. Given the good agreement between data and simulated events as illustrated in Figure 3, the simulated effective area is used to evaluate the expected signal (see Section 4). The expected background is estimated from the scrambled data (randomising the UTC time of the selected events) in order to minimise the effect of systematic uncertainties from the simulation.

#### 4 Optimisation of the event selection criteria

The data set used in this analysis comprises a total of 2693 runs recorded between the 27<sup>th</sup> of January 2007 and the 31<sup>st</sup> of December 2008, corresponding to a total livetime of 294.6 days, without taking into account the period in which the Sun was below the horizon. The detector consisted of 5 lines for most of 2007 and of 9, 10 and 12 lines during 2008, with a corresponding total livetime of 134.6, 38.0, 39.0 and 83.0 days respectively.

Only upgoing events are kept in the analysis. The track fit is required to use a number of hits greater than five in at least two lines in order to ensure a non-degenerate 5-parameter fit with an accurate reconstruction of the azimuth angle.

The UTC time of the events is uniformly randomised in the data-taking period in order to estimate the background in the Sun’s direction from the data itself. The zenith and azimuth angles of the reconstructed tracks are kept so as to preserve the angular response of the detector in the optimisation of the selection criteria. This procedure provides a means to follow a data blinding strategy while using all the relevant information on the detector performance.

The values of the parameters used in the event selection criteria, the quality parameter,  $Q$  (see Equation 2.1), and the angular separation between tracks and the Sun’s direction,  $\Psi$ , are chosen so as to optimise the model rejection factor [38]. For each WIMP mass and each annihilation channel, the chosen individual values  $Q_{\text{cut}}$  and  $\Psi_{\text{cut}}$  are those that minimise the average 90% confidence level (CL) upper limit on the  $\nu_\mu + \bar{\nu}_\mu$  flux,  $\bar{\Phi}_{\nu_\mu + \bar{\nu}_\mu}$ , defined as

$$\bar{\Phi}_{\nu_\mu + \bar{\nu}_\mu} = \frac{\bar{\mu}^{90\%}}{\sum_i \bar{A}_{\text{eff}}^i(M_{\text{WIMP}}) \times T_{\text{eff}}^i}, \quad (4.1)$$

where the index  $i$  denotes the periods with different detector configurations (5, 9, 10 and 12 detection lines),  $\bar{\mu}^{90\%}$  is the average upper limit of the background at 90% CL computed using a Poisson distribution in the Feldman-Cousins approach [39] (for consistency in the comparison with other neutrino experiments limits computation) and  $T_{\text{eff}}^i$  is the total livetime for each detector configuration. The effective area averaged over the neutrino energy,  $\bar{A}_{\text{eff}}^i(M_{\text{WIMP}})$ , is defined as:

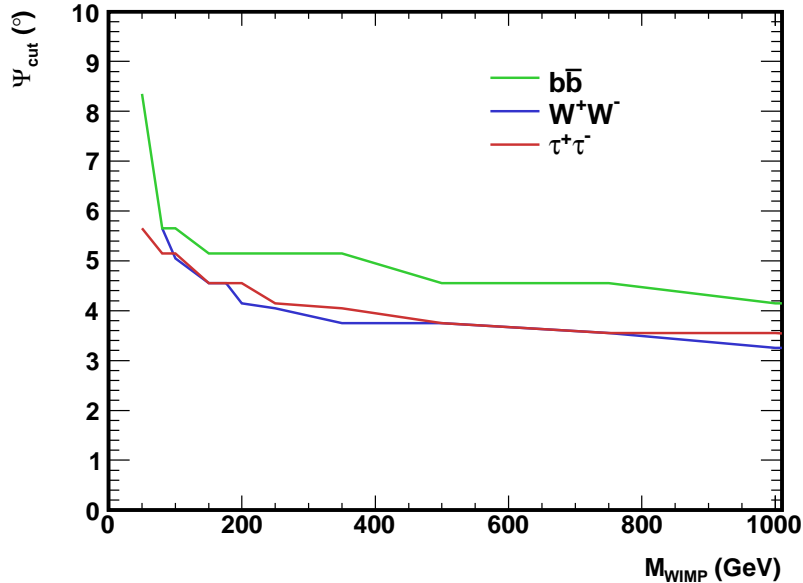


**Figure 4.** Optimum angular separation  $\Psi_{\text{cut}}$  between the muon tracks and the Sun's direction for  $Q_{\text{cut}} = 1.4$  as a function of the WIMP mass for the self-annihilation channels  $b\bar{b}$  (green),  $W^+W^-$  (blue) and  $\tau^+\tau^-$  (red).

$$\bar{A}_{\text{eff}}^i(M_{\text{WIMP}}) = \sum_{\nu, \bar{\nu}} \left( \frac{\int_{E_{\nu}^{\text{th}}}^{M_{\text{WIMP}}} A_{\text{eff}}^i(E_{\nu, \bar{\nu}}) \frac{dN_{\nu, \bar{\nu}}}{dE_{\nu, \bar{\nu}}} dE_{\nu, \bar{\nu}}}{\int_0^{M_{\text{WIMP}}} \frac{dN_{\nu}}{dE_{\nu}} dE_{\nu} + \frac{dN_{\bar{\nu}}}{dE_{\bar{\nu}}} dE_{\bar{\nu}}} \right), \quad (4.2)$$

where  $E_{\nu}^{\text{th}} = 10$  GeV is the energy threshold for neutrino detection in ANTARES,  $M_{\text{WIMP}}$  is the WIMP mass,  $dN_{\nu, \bar{\nu}}/dE_{\nu, \bar{\nu}}$  is the energy spectrum of the (anti-)neutrinos at the surface of the Earth as shown in Figure 2 (top), and  $A_{\text{eff}}(E_{\nu, \bar{\nu}})$  is the effective area of ANTARES as a function of the (anti-)neutrino energy for tracks coming from the direction of the Sun below the horizon. Due to their different cross-sections, the effective areas for neutrinos and anti-neutrinos are slightly different and therefore are considered separately. In addition, the fluxes of muon neutrinos and anti-neutrinos from the Sun are different and are convoluted with their respective efficiencies.

An example of an averaged effective area  $\bar{A}_{\text{eff}}(M_{\text{WIMP}})$  for this analysis is shown in Figure 2 (bottom) for  $(Q_{\text{cut}}, \Psi_{\text{cut}}) = (1.4, 3^\circ)$  with the visibility of the Sun taken into account, and a detector in a 12 line configuration. Whilst the values for each configuration of the detector are detailed in Tables 1 and 2 for optimised  $(Q_{\text{cut}}, \Psi_{\text{cut}})$  (see section 4). The corresponding  $\bar{A}_{\text{eff}}(M_{\text{WIMP}})$  distribution of the  $W^+W^-$  channel is kinematically allowed for  $M_{\text{WIMP}} > M_W = 80.4$  GeV [2]. Note that even though the sensitivity  $\bar{A}_{\text{eff}}(M_{\text{WIMP}})$  decreases rapidly with a decreasing WIMP mass, the low mass region,  $50 \text{ GeV} < M_{\text{WIMP}} < 100 \text{ GeV}$ , can still be probed.

The cut optimisation procedure provides a pair of optimised values,  $Q$  and  $\Psi$ , for each mass of the WIMP and for each studied channel. A value of  $Q_{\text{cut}} = 1.4$  is found optimum

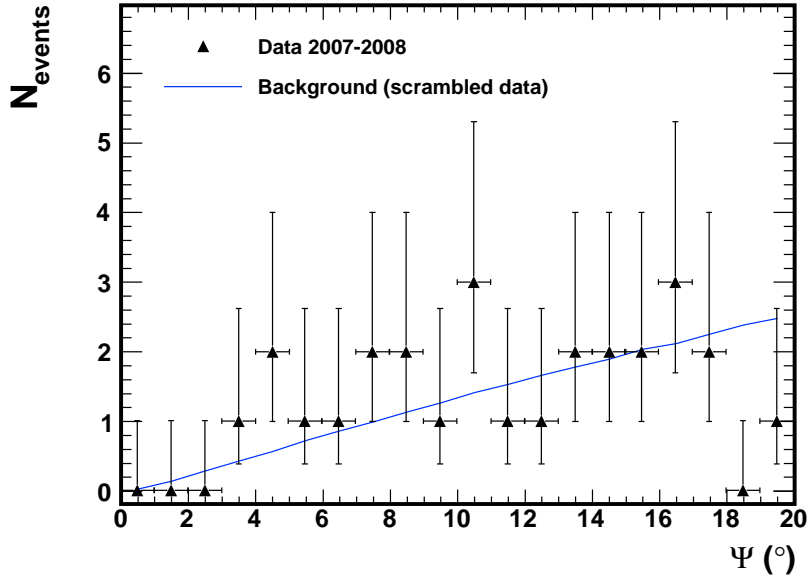


**Figure 5.** Differential distribution of the angular separation  $\Psi$  of the event tracks with respect to the Sun’s direction for the expected background (solid blue line) compared to the data (black triangles). A  $1\sigma$  Poisson uncertainty is shown for each data point.

for all considered masses and channels. The distribution of the optimal angular separation around the Sun,  $\Psi_{\text{cut}}$ , as a function of the WIMP mass is shown in Figure 4. As the  $b\bar{b}$  channel has a softer energy spectrum,  $\Psi_{\text{cut}}$  is larger for this channel. For all the channels,  $\Psi_{\text{cut}}$  is larger in the low mass regime because of a worse angular resolution at low energy ( $E_\nu < 100$  GeV). After the optimised  $Q_{\text{cut}}$  and  $\Psi_{\text{cut}}$  are fixed, the data sample is unblinded.

## 5 Results and discussion

Figure 5 shows the distribution of the angular separation between the events and the Sun’s direction obtained after applying the selection criteria on the zenith angle, the minimum number of hits and lines, and a  $Q_{\text{cut}} = 1.4$ . A total of 27 events are found within a  $20^\circ$  angular separation. No statistically significant excess is observed above the scrambled background in the Sun’s direction.

Using the values for the cuts obtained in the optimisation procedure, 90% CL limits on the  $\nu_\mu + \bar{\nu}_\mu$  flux,  $\Phi_{\nu_\mu + \bar{\nu}_\mu}$ , can be computed from the data according to Equation 4.1, where the  $\bar{\mu}^{90\%}$  average 90% CL upper limit is replaced by the upper limit at 90% CL,  $\mu^{90\%}$ , on the number of observed events. The corresponding limits are presented in Figure 6 (top) for the three representative self-annihilation channels  $b\bar{b}$ ,  $W^+W^-$  and  $\tau^+\tau^-$ . Given its soft energy spectrum (see Figure 2 (top)), the channel  $b\bar{b}$  yields the weakest limit, while the others ( $W^+W^-$ ,  $\tau^+\tau^-$ ) are the most stringent.

The corresponding limits on the muon flux are calculated using a conversion factor between the neutrino and the muon fluxes ( $\Phi_\mu = \Gamma_{\nu \rightarrow \mu} \times \Phi_{\nu_\mu + \bar{\nu}_\mu}$ ) computed using the package DarkSUSY [40]. Figure 6 (bottom) shows the 90% CL muon flux limits,  $\Phi_\mu$ , for the channels

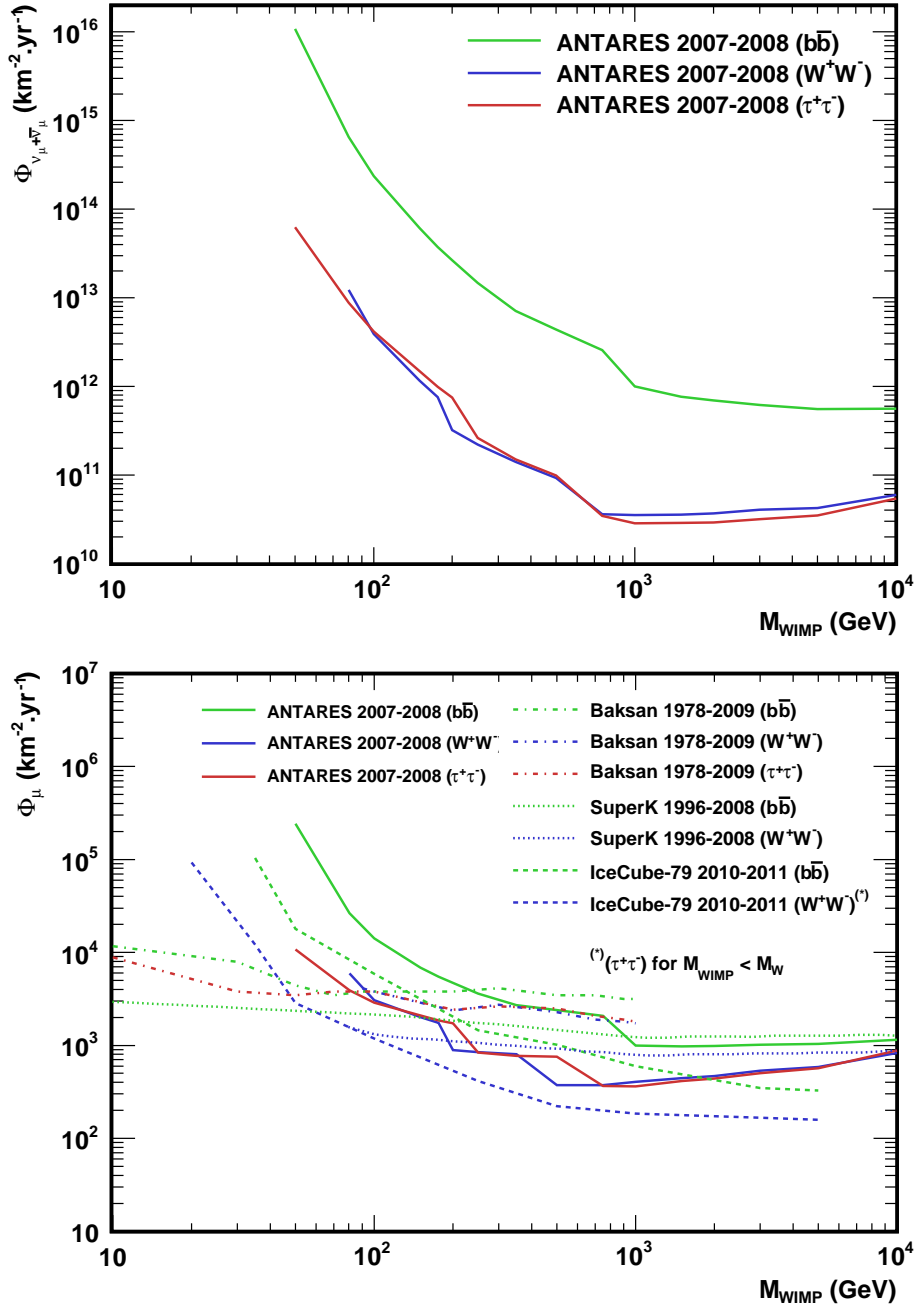


**Figure 6. Top:** 90% CL upper limits on the neutrino plus anti-neutrino flux as a function of the WIMP mass in the range  $M_{\text{WIMP}} \in [50 \text{ GeV}; 10 \text{ TeV}]$  for the three self-annihilation channels  $b\bar{b}$  (green),  $W^+W^-$  (blue),  $\tau^+\tau^-$  (red). **Bottom:** 90% CL upper limit on the muon flux as a function of the WIMP mass in the range  $M_{\text{WIMP}} \in [50 \text{ GeV}; 10 \text{ TeV}]$  for the three self-annihilation channels  $b\bar{b}$  (green),  $W^+W^-$  (blue) and  $\tau^+\tau^-$  (red). The results from Baksan 1978 – 2009 [41] (dash-dotted lines), Super-Kamiokande 1996 – 2008 [42] (dotted lines) and IceCube-79 2010 – 2011 [43] (dashed lines) are also shown.

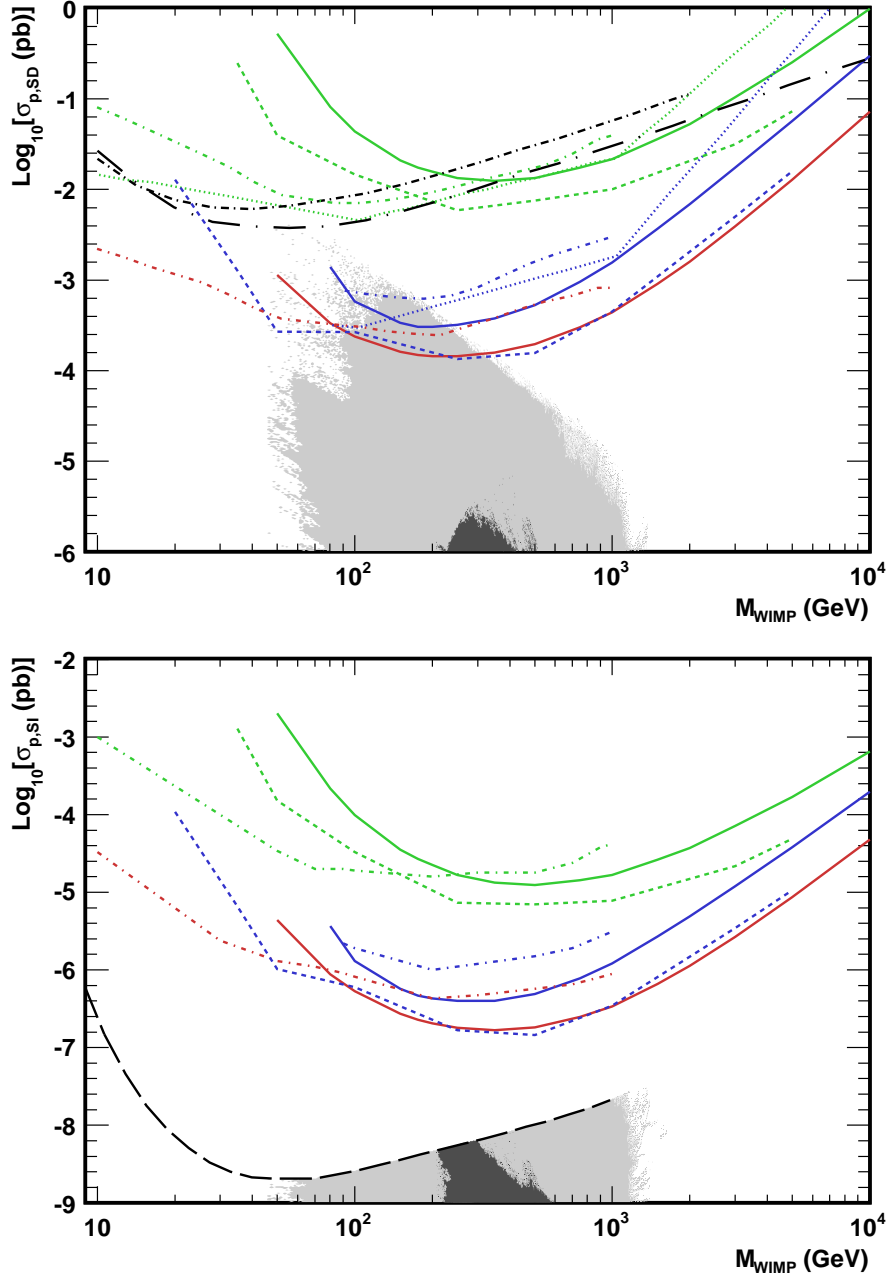


**Figure 7.** 90% CL upper limits on the SD and SI WIMP-proton cross-sections (upper and lower plots, respectively) as a function of the WIMP mass, for the three self-annihilation channels:  $b\bar{b}$  (green),  $W^+W^-$  (blue) and  $\tau^+\tau^-$  (red), for ANTARES 2007-2008 (solid line) compared to the results of other indirect search experiments: Baksan 1978 – 2009 [41] (dash-dotted lines), Super-Kamiokande 1996 – 2008 [42] (dotted lines) and IceCube-79 2010 – 2011 [43] (dashed lines) and the result of the most stringent direct search experiments (black): SIMPLE 2004 – 2011 [46] (short dot-dashed line in upper plot), COUPP 2010 – 2011 [47] (long dot-dashed line in upper plot) and XENON100 2011 – 2012 [48] (dashed line in lower plot). The results of a grid scan of the CMSSM and MSSM-7 are included (dark and light grey shaded areas respectively) for the sake of comparison.

$b\bar{b}$ ,  $W^+W^-$  and  $\tau^+\tau^-$ . The latest results from Baksan [41], Super-Kamiokande [42] and IceCube-79 [43] are also shown for comparison.

Assuming equilibrium between the WIMP capture and self-annihilation rates in the Sun, the limits on the spin-dependent (SD) and the spin-independent (SI) WIMP-proton scattering cross-sections are derived for the case in which one or the other is dominant.

The Sun is considered to be free in the galactic halo [44]. A local dark matter density of  $0.3 \text{ GeV/cm}^3$  and a Maxwellian velocity distribution of the WIMP with a RMS velocity of  $270 \text{ km/s}$  are assumed [2], and no additional dark matter disk that could enhance the local dark matter density is considered (see Reference [45] for a discussion).

The 90% CL limits for the SD,  $\sigma_{p,\text{SD}}$ , and SI,  $\sigma_{p,\text{SI}}$ , WIMP-proton cross-sections derived for the signal channels  $b\bar{b}$ ,  $W^+W^-$  and  $\tau^+\tau^-$  are presented in Figure 7. The latest results from Baksan [41], Super-Kamiokande [42] and IceCube-79 [43] together with the latest and the most stringent limits from the direct search experiments SIMPLE [46], COUPP [47] and XENON100 [48] are shown. The allowed parameter space from the CMSSM and MSSM-7 models according to the results from an adaptative grid scan performed with DarkSUSY are also shown. For CMSSM and MSSM-7, their free parameters are limited as shown in Table 3. All the limits presented in Figure 7 are computed with a muon energy threshold at  $E_\mu = 1 \text{ GeV}$ . For this figure the shaded regions show a grid scan of the model parameter space, taking into account the latest constraints for various observables from accelerator-based experiments shown in Table 4, in particular the results on the Higgs boson mass from ATLAS and CMS,  $M_h = 125 \pm 2 \text{ GeV}$  [49], and the latest limit on the SI WIMP-proton scattering cross-section by XENON100 [48]. A relatively loose constraint on the neutralino relic density  $0 < \Omega_{\text{CDM}}h^2 < 0.1232$  [6] is used to take into account the existence of other possible types of dark matter particles.

All the results are summarised in Tables 5 and 6, where for each WIMP mass and channel the values of the optimised angular separation, the average 90% CL upper limit computed from the background without signal expectation, the 90% CL upper limit on the number of observed events, the total averaged effective area and the 90% CL upper limits are presented. Systematic uncertainties are taken into account and included in the evaluation of the limits using the PoLe software following the approach detailed in Reference [50]. The total systematic uncertainty on the detector efficiency is around 20% and comes mainly from the uncertainties on the average quantum efficiency of the PMTs as well as the angular acceptance and the sea water absorption length ( $\pm 10\%$  for all of them). The detailed uncertainties study is described in Reference [23]. This total systematic uncertainty translates into a degradation of the upper limit between 3% and 6%, depending on the WIMP mass.

The neutrino flux due to WIMP annihilation in the Sun is highly dependent on the capture rate of WIMPs in the core of the Sun, which in turn is dominated by the SD WIMP-proton cross-section. This makes these indirect searches better compared to direct search experiments. This is not the case for the SI WIMP-proton cross-section, where the limits coming from direct search experiments like XENON100 are better thanks to their target materials.

Using the first two years of data recorded by the ANTARES neutrino telescope, an indirect search for dark matter towards the Sun has been performed. The observed number of neutrino events in the Sun's direction is compatible with the expectation from the atmospheric backgrounds. The derived limits are comparable with those obtained by other neutrino observatories and are more stringent than those obtained by direct search experiments

for the spin-dependent WIMP-proton scattering cross-section thanks to the hard channels ( $W^+W^-$ ,  $\tau^+\tau^-$ ). The present ANTARES limits already begin to constrain the parameter spaces of the MSSM-7 model.

## Acknowledgments

The authors acknowledge the financial support of the funding agencies: Centre National de la Recherche Scientifique (CNRS), Commissariat à l'énergie atomique et aux énergies alternatives (CEA), Agence National de la Recherche (ANR), Commission Européenne (FEDER fund and Marie Curie Program), Région Alsace (contrat CPER), Région Provence-Alpes-Côte d'Azur, Département du Var and Ville de La Seyne-sur-Mer, France; Bundesministerium für Bildung und Forschung (BMBF), Germany; Istituto Nazionale di Fisica Nucleare (INFN), Italy; Stichting voor Fundamenteel Onderzoek der Materie (FOM), Nederlandse organisatie voor Wetenschappelijk Onderzoek (NWO), the Netherlands; Council of the President of the Russian Federation for young scientists and leading scientific schools supporting grants, Russia; National Authority for Scientific Research (ANCS), Romania; Ministerio de Ciencia e Innovación (MICINN), Prometeo of Generalitat Valenciana and MultiDark, Spain; Agence de l'Oriental and CNRST, Morocco. We also acknowledge the technical support of Ifremer, AIM and Foselev Marine for the sea operation and the CC-IN2P3 for the computing facilities.

## References

- [1] G. Bertone, D. Hooper, J. Silk, *Particle Dark Matter: Evidence, Candidates and Constraints*, Phys. Rept., 2005, **405**: pp. 279-390.
- [2] J. Beringer et al., Particle Data Group, Phys. Rev. D **86**, 010001 (2012).
- [3] F. Zwicky, *Die Rotverschiebung von extragalaktischen Nebeln*, Helv. Phys. Acta **6**, 110 (1933).
- [4] W. J. de Blok, S. S. McGaugh, A. Bosma and V. C. Rubin., *Mass density profiles of LSB galaxies*, Astrophys. J. 552 (2001) L23-L26.
- [5] D. Clowe et al., *A direct empirical proof of the existence of dark matter*, Astrophys. J. 648 (2006) L109-L113.
- [6] E. Komatsu et al., WMAP Collaboration, *Seven-Year Wilkinson Microwave Anisotropy Probe (WMAP) Observations: Cosmological Interpretation*, Astrophys. J. Suppl. 192 (2011) 18.
- [7] J.R. Ellis et al., *Supersymmetric relics from the big bang*, Nucl. Phys. B **238**, 453 (1984).
- [8] H. Goldberg et al., *Constraint on the Photino Mass from Cosmology*, Phys. Rev. Lett. **50**, 1419 (1983).
- [9] J. Ellis et al., *Neutrino Fluxes from CMSSM LSP Annihilations in the Sun*, Phys. Rev. D **81**, 085004 (2010).
- [10] L. Bergström and P. Gondolo, *Limits on direct detection of neutralino dark matter from  $b \rightarrow s\gamma$  decays*, Astropart. Phys. **5** (1996) 263-278.
- [11] A. Gould, *Direct And Indirect Capture Of Wimps By The Earth*, Astrophys. J. **328**, 919 (1988); T. K. Gaisser, G. Steigman, and S. Tilav, *Limits on Cold Dark Matter Candidates from Deep Underground Detectors*, Phys. Rev. D **34**, 2206 (1986); J. Silk et al., *The Photino, the Sun and High-Energy Neutrinos*, Phys. Rev. Lett. **55**, 257 (1985); W. H. Press and D. N. Spergel, *Capture by the sun of a galactic population of weakly interacting, massive particles*, Astrophys. J. **296**, 679 (1985).

- [12] A. Gould, *Resonant enhancements in weakly interacting massive particle capture by the earth*, *Astrophys. J.* **321**, 571 (1987).
- [13] M. Ageron et al., ANTARES Collaboration, *ANTARES: the first undersea neutrino telescope*, *Nucl. Inst. and Meth. in Phys. Res. A* **656** (2011) 11-38.
- [14] P. Amram, ANTARES Collaboration, *The ANTARES optical module*, *Nucl. Inst. and Meth. in Phys. Res. A* **484** (2002) 369.
- [15] J.A. Aguilar et al., ANTARES Collaboration, *Study of large hemispherical photomultiplier tubes for the ANTARES neutrino telescope*, *Nucl. Inst. and Meth. in Phys. Res. A* **555** (2005) 132.
- [16] J.A. Aguilar et al., ANTARES Collaboration, *Performance of the front-end electronics of the ANTARES Neutrino Telescope*, *Nucl. Inst. and Meth. in Phys. Res. A* **622** (2010) 59.
- [17] J.A. Aguilar et al., ANTARES Collaboration, *The data acquisition system for the ANTARES neutrino telescope*, *Nucl. Inst. and Meth. in Phys. Res. A* **570** (2007) 107.
- [18] P. Amram, ANTARES Collaboration, *Sedimentation and Fouling of Optical Surfaces at the ANTARES Site*, *Astropart. Phys.* **19** (2003) 253.
- [19] J.A. Aguilar et al., ANTARES Collaboration, *AMADEUS - The Acoustic Neutrino Detection Test System of the ANTARES Deep-Sea Neutrino Telescope*, *Nucl. Inst. and Meth. in Phys. Res. A* **626-627** (2011) 128.
- [20] J.A. Aguilar et al., *First results of the Instrumentation Line for the deep-sea ANTARES neutrino telescope*, ANTARES Collaboration, *Astropart. Phys.* **26** (2006) 314.
- [21] S. Adrián-Martínez et al., *The positioning system of the ANTARES Neutrino Telescope*, ANTARES Collaboration, *JINST* **7** (2012) T08002.
- [22] M. Ageron et al., ANTARES Collaboration, *The Antares optical beacon system*, *Nucl. Inst. and Meth. in Phys. Res. A* **578** (2007) 498.
- [23] J.A. Aguilar et al., ANTARES Collaboration, *Time Calibration of the ANTARES neutrino Telescope*, *Astropart. Phys.* **34** (2011) 539.
- [24] J.A. Aguilar et al., ANTARES Collaboration, *Search for a diffuse flux of high energy  $n_\mu$  with the ANTARES neutrino telescope*, *Phys. Lett.* **B696** (2011) 16.
- [25] S. Adrián-Martínez et al., ANTARES Collaboration, *First search for point sources of high energy cosmic neutrinos with the ANTARES neutrino telescope*, *Ap. J. Letter* **743** (2011) L14.
- [26] S. Adrián-Martínez et al., ANTARES Collaboration, *Search for relativistic magnetic monopoles with the ANTARES neutrino telescope*, *Astropart. Phys.* **35** (2012) 634.
- [27] J.A. Aguilar et al., ANTARES Collaboration, *A fast algorithm for muon track reconstruction and its application to the ANTARES neutrino Telescope*, *Astropart. Phys.* **34** (2011) 652.
- [28] J. Edsjö, <http://www.physto.se/edsjo/wimpsim/>.
- [29] R. Abbasi et al., IceCube Collaboration, *Limits on a Muon Flux from Neutralino Annihilations in the Sun with the IceCube 22-String Detector*, *Phys. Rev. Lett.* **102**, 201302 (2009).
- [30] M. M. Boliev et al., Baksan Collaboration, *Search for supersymmetric dark matter with Baksan Underground telescope*, *Nucl. Phys. B, Proc. Suppl.* **48**, 83 (1996).
- [31] M. Ambrosio et al., MACRO Collaboration, *Limits on Dark Matter Wimps using Upward Going Muons in the MACRO Detector*, *Phys. Rev. D* **60**, 082002 (1999).
- [32] S. Desai et al., Super-Kamiokande Collaboration, *Search for dark matter wimps using upward through-going muons in Super-Kamiokande*, *Phys. Rev. D* **70**, 083523 (2004).
- [33] M. Ackermann et al., AMANDA Collaboration, *Limits to the muon flux from neutralino annihilations in the Sun with the AMANDA detector*, *Astropart. Phys.* **24** (2006) 459.



- [34] D. Heck et al., Report FZKA 6019 (1998), Forschungszentrum Karlsruhe; D. Heck and J. Knapp, Report FZKA 6097 (1998), Forschungszentrum Karlsruhe.
- [35] G. Barr et al., *Flux of atmospheric neutrinos*, Phys. Rev. D **39**, 3532 (1989); V. Agrawal et al., *Atmospheric neutrino flux above 1 GeV*, Phys. Rev. D **53**, 1314 (1996).
- [36] J.A. Aguilar et al., ANTARES Collaboration, *Transmission of light in deep sea water at the site of the Antares neutrino telescope*, Astropart. Phys. **23** (2005) 131.
- [37] C. Hettlage et al., *The sun as a high energy neutrino source*, Astropart.Phys. **13** (2000) 45-50.
- [38] G.C. Hill, K. Rawlins, *Unbiased cut selection for optimal upper limits in neutrino detectors: the model rejection potential technique*, Astropart. Phys. **19** (2003) 393-402.
- [39] G.J. Feldman, R.D. Cousins, *A Unified Approach to the Classical Statistical Analysis of Small Signals*, Phys. Rev. D **57**, 3873-3889 (1998).
- [40] P. Gondolo et al., *DarkSUSY: Computing Supersymmetric Dark Matter Properties Numerically*, J. Cosm. and Astropart. Phys., JCAP07, 008 (2004).
- [41] M.M. Boliev et al., Baksan Collaboration, *Search for muon signal from dark matter annihilations in the Sun with the Baksan Underground Scintillator Telescope for 24.12 years* [astro-ph/1301.1138].
- [42] T. Tanaka et al., Super-Kamiokande Collaboration, *An Indirect Search for WIMPs in the Sun using 3109.6 days of upward-going muons in Super-Kamiokande*, Astrophys. J. **742**, 78 (2011).
- [43] M.G. Aartsen et al., IceCube Collaboration, *Search for dark matter annihilations in the Sun with the 79-string IceCube detector*, [astro-ph/1212.4097].
- [44] S. Sivertsson and J. Edsjö, *WIMP diffusion in the Solar System including Solar WIMP-nucleon scattering*, Phys. Rev. D **85**, 123514 (2012).
- [45] G. Wikström and J. Edsjö, *Limits on the WIMP-nucleon scattering cross-section from neutrino telescopes*, J. Cosm. and Astropart. Phys., JCAP04, 009 (2009).
- [46] M. Felizardo et al., SIMPLE Collaboration, *Final Analysis and Results of the Phase II SIMPLE Dark Matter Search*, Phys. Rev. Lett. **108**, 201302 (2012).
- [47] E. Behnke et al., COUPP Collaboration, *First dark matter search results from a 4-kg CF<sub>3</sub>I bubble chamber operated in a deep underground site*, Phys. Rev. D **86**, 052001 (2012).
- [48] E. Aprile et al., XENON Collaboration, *Dark Matter Results from 225 Live Days of XENON100 Data*, [astro-ph/1207.5988].
- [49] O. Buchmueller et al., *The CMSSM and NUHM1 in Light of 7 TeV LHC, B<sub>s</sub> to mu+mu- and XENON100 Data*, [hep-ph/1207.7315].
- [50] F. Tegenfeldt, J. Conrad, *On Bayesian Treatment of Systematic Uncertainties In Confidence Interval Calculation*, Nucl. Inst. and Meth. in Phys. Res. A **539** (2005) 407-413; J. Conrad et al., *Including Systematic Uncertainties in Confidence Interval Construction for Poisson Statistics*, Phys. Rev. D **67**, 012002 (2003); J. Conrad, *Discovery and Upper Limits in Search for Exotic Physics with Neutrino Telescopes*, [astro-ph/0612082].

$M_{\text{WIMP}}$ (GeV)	Channel	$\bar{A}_{\text{eff}}^{5\text{L}}(M_{\text{WIMP}})$ (m <sup>2</sup> )	$\bar{A}_{\text{eff}}^{9\text{L}}(M_{\text{WIMP}})$ (m <sup>2</sup> )	$\bar{A}_{\text{eff}}^{10\text{L}}(M_{\text{WIMP}})$ (m <sup>2</sup> )	$\bar{A}_{\text{eff}}^{12\text{L}}(M_{\text{WIMP}})$ (m <sup>2</sup> )
50	$b\bar{b}$	$3.5 \times 10^{-10}$	$7.3 \times 10^{-10}$	$1.2 \times 10^{-9}$	$1.6 \times 10^{-9}$
	$\tau\bar{\tau}$	$5.5 \times 10^{-8}$	$1.0 \times 10^{-7}$	$1.3 \times 10^{-7}$	$1.6 \times 10^{-7}$
80.3	$b\bar{b}$	$5.4 \times 10^{-9}$	$9.9 \times 10^{-9}$	$1.3 \times 10^{-8}$	$1.5 \times 10^{-8}$
	$W^+W^-$	$2.7 \times 10^{-7}$	$4.7 \times 10^{-7}$	$5.9 \times 10^{-7}$	$9.0 \times 10^{-7}$
	$\tau\bar{\tau}$	$3.7 \times 10^{-7}$	$6.8 \times 10^{-7}$	$9.6 \times 10^{-7}$	$1.4 \times 10^{-6}$
100	$b\bar{b}$	$1.4 \times 10^{-8}$	$2.5 \times 10^{-8}$	$3.4 \times 10^{-8}$	$4.4 \times 10^{-8}$
	$W^+W^-$	$8.2 \times 10^{-7}$	$1.6 \times 10^{-6}$	$2.2 \times 10^{-6}$	$3.2 \times 10^{-6}$
	$\tau\bar{\tau}$	$7.5 \times 10^{-7}$	$1.4 \times 10^{-6}$	$2.1 \times 10^{-6}$	$3.0 \times 10^{-6}$
150	$b\bar{b}$	$5.5 \times 10^{-8}$	$9.9 \times 10^{-8}$	$1.4 \times 10^{-7}$	$2.0 \times 10^{-7}$
	$W^+W^-$	$2.8 \times 10^{-6}$	$4.9 \times 10^{-6}$	$8.4 \times 10^{-6}$	$1.2 \times 10^{-5}$
	$\tau\bar{\tau}$	$2.2 \times 10^{-6}$	$3.9 \times 10^{-6}$	$6.5 \times 10^{-6}$	$9.2 \times 10^{-6}$
176	$b\bar{b}$	$8.7 \times 10^{-8}$	$1.6 \times 10^{-7}$	$2.3 \times 10^{-7}$	$3.2 \times 10^{-7}$
	$W^+W^-$	$4.2 \times 10^{-6}$	$7.5 \times 10^{-6}$	$1.3 \times 10^{-5}$	$1.8 \times 10^{-5}$
	$\tau\bar{\tau}$	$3.2 \times 10^{-6}$	$5.8 \times 10^{-6}$	$9.8 \times 10^{-6}$	$1.4 \times 10^{-5}$
200	$b\bar{b}$	$1.2 \times 10^{-7}$	$2.2 \times 10^{-7}$	$3.2 \times 10^{-7}$	$4.6 \times 10^{-7}$
	$W^+W^-$	$5.3 \times 10^{-6}$	$9.4 \times 10^{-6}$	$1.6 \times 10^{-5}$	$2.2 \times 10^{-5}$
	$\tau\bar{\tau}$	$4.3 \times 10^{-6}$	$7.7 \times 10^{-6}$	$1.3 \times 10^{-5}$	$1.8 \times 10^{-5}$
250	$b\bar{b}$	$2.1 \times 10^{-7}$	$3.9 \times 10^{-7}$	$5.9 \times 10^{-7}$	$8.4 \times 10^{-7}$
	$W^+W^-$	$7.9 \times 10^{-6}$	$1.3 \times 10^{-5}$	$2.5 \times 10^{-5}$	$3.3 \times 10^{-5}$
	$\tau\bar{\tau}$	$6.5 \times 10^{-6}$	$1.1 \times 10^{-5}$	$2.0 \times 10^{-5}$	$2.7 \times 10^{-5}$
350	$b\bar{b}$	$4.3 \times 10^{-7}$	$7.9 \times 10^{-7}$	$1.2 \times 10^{-6}$	$1.7 \times 10^{-6}$
	$W^+W^-$	$1.3 \times 10^{-5}$	$2.2 \times 10^{-5}$	$4.0 \times 10^{-5}$	$5.4 \times 10^{-5}$
	$\tau\bar{\tau}$	$1.2 \times 10^{-5}$	$2.0 \times 10^{-5}$	$3.6 \times 10^{-5}$	$4.8 \times 10^{-5}$

**Table 1.** Detailed numerical values of the averaged effective areas  $\bar{A}_{\text{eff}}^i(M_{\text{WIMP}})$  for the signal of WIMP self-annihilation inside the Sun,  $b\bar{b}$ ,  $W^+W^-$  and  $\tau^+\tau^-$  channels. The 5, 9, 10 and 12 line configurations (i index) with  $(Q_{\text{cut}}, \Psi_{\text{cut}})$  after optimisation (see section 4) are considered. The total averaged effective area  $\bar{A}_{\text{eff}}(M_{\text{WIMP}}) = \sum_i \bar{A}_{\text{eff}}^i(M_{\text{WIMP}}) \times T_{\text{eff}}^i$  (see Equation 4.2) is reported in Tables 5 and 6. Results for  $M_{\text{WIMP}} > 350$  GeV are available in Table 2.

$M_{\text{WIMP}}$ (GeV)	Channel	$\bar{A}_{\text{eff}}^{5\text{L}}(M_{\text{WIMP}})$ (m <sup>2</sup> )	$\bar{A}_{\text{eff}}^{9\text{L}}(M_{\text{WIMP}})$ (m <sup>2</sup> )	$\bar{A}_{\text{eff}}^{10\text{L}}(M_{\text{WIMP}})$ (m <sup>2</sup> )	$\bar{A}_{\text{eff}}^{12\text{L}}(M_{\text{WIMP}})$ (m <sup>2</sup> )
500	$b\bar{b}$	$7.5 \times 10^{-7}$	$1.3 \times 10^{-6}$	$2.2 \times 10^{-6}$	$3.1 \times 10^{-6}$
	$W^+W^-$	$1.9 \times 10^{-5}$	$3.4 \times 10^{-5}$	$5.9 \times 10^{-5}$	$8.0 \times 10^{-5}$
	$\tau\bar{\tau}$	$1.9 \times 10^{-5}$	$3.2 \times 10^{-5}$	$5.7 \times 10^{-5}$	$7.6 \times 10^{-5}$
750	$b\bar{b}$	$1.3 \times 10^{-6}$	$2.2 \times 10^{-6}$	$3.8 \times 10^{-6}$	$5.2 \times 10^{-6}$
	$W^+W^-$	$2.6 \times 10^{-5}$	$4.5 \times 10^{-5}$	$7.8 \times 10^{-5}$	$1.0 \times 10^{-4}$
	$\tau\bar{\tau}$	$2.7 \times 10^{-5}$	$4.6 \times 10^{-5}$	$8.1 \times 10^{-5}$	$1.1 \times 10^{-4}$
1000	$b\bar{b}$	$1.7 \times 10^{-6}$	$3.0 \times 10^{-6}$	$5.2 \times 10^{-6}$	$7.1 \times 10^{-6}$
	$W^+W^-$	$2.7 \times 10^{-5}$	$4.8 \times 10^{-5}$	$8.3 \times 10^{-5}$	$1.1 \times 10^{-4}$
	$\tau\bar{\tau}$	$3.2 \times 10^{-5}$	$5.6 \times 10^{-5}$	$9.8 \times 10^{-5}$	$1.3 \times 10^{-4}$
1500	$b\bar{b}$	$2.3 \times 10^{-6}$	$4.0 \times 10^{-6}$	$7.0 \times 10^{-6}$	$9.4 \times 10^{-6}$
	$W^+W^-$	$2.7 \times 10^{-5}$	$4.8 \times 10^{-5}$	$8.4 \times 10^{-5}$	$1.1 \times 10^{-4}$
	$\tau\bar{\tau}$	$3.3 \times 10^{-5}$	$5.9 \times 10^{-5}$	$1.0 \times 10^{-4}$	$1.3 \times 10^{-4}$
2000	$b\bar{b}$	$2.7 \times 10^{-6}$	$4.5 \times 10^{-6}$	$8.2 \times 10^{-6}$	$1.1 \times 10^{-5}$
	$W^+W^-$	$2.6 \times 10^{-5}$	$4.6 \times 10^{-5}$	$8.1 \times 10^{-5}$	$1.1 \times 10^{-4}$
	$\tau\bar{\tau}$	$3.3 \times 10^{-5}$	$5.8 \times 10^{-5}$	$1.0 \times 10^{-4}$	$1.4 \times 10^{-4}$
3000	$b\bar{b}$	$3.0 \times 10^{-6}$	$5.1 \times 10^{-6}$	$9.3 \times 10^{-6}$	$1.2 \times 10^{-5}$
	$W^+W^-$	$2.4 \times 10^{-5}$	$4.2 \times 10^{-5}$	$7.4 \times 10^{-5}$	$9.7 \times 10^{-5}$
	$\tau\bar{\tau}$	$3.0 \times 10^{-5}$	$5.4 \times 10^{-5}$	$9.5 \times 10^{-5}$	$1.2 \times 10^{-4}$
5000	$b\bar{b}$	$3.5 \times 10^{-6}$	$5.8 \times 10^{-6}$	$1.0 \times 10^{-5}$	$1.3 \times 10^{-5}$
	$W^+W^-$	$2.2 \times 10^{-5}$	$3.9 \times 10^{-5}$	$6.6 \times 10^{-5}$	$8.6 \times 10^{-5}$
	$\tau\bar{\tau}$	$2.7 \times 10^{-5}$	$4.8 \times 10^{-5}$	$8.0 \times 10^{-5}$	$1.0 \times 10^{-4}$
10000	$b\bar{b}$	$3.5 \times 10^{-6}$	$5.5 \times 10^{-6}$	$9.9 \times 10^{-6}$	$1.3 \times 10^{-5}$
	$W^+W^-$	$1.6 \times 10^{-5}$	$2.8 \times 10^{-5}$	$4.9 \times 10^{-5}$	$6.5 \times 10^{-5}$
	$\tau\bar{\tau}$	$1.8 \times 10^{-5}$	$3.1 \times 10^{-5}$	$5.4 \times 10^{-5}$	$7.2 \times 10^{-5}$

**Table 2.** Detailed numerical values of the averaged effective areas  $\bar{A}_{\text{eff}}^i(M_{\text{WIMP}})$  for the signal of WIMP self-annihilation inside the Sun,  $b\bar{b}$ ,  $W^+W^-$  and  $\tau^+\tau^-$  channels. The 5, 9, 10 and 12 line configurations ( $i$  index) with  $(Q_{\text{cut}}, \Psi_{\text{cut}})$  after optimisation (see section 4) are considered. The total averaged effective area  $\bar{A}_{\text{eff}}(M_{\text{WIMP}}) = \sum_i \bar{A}_{\text{eff}}^i(M_{\text{WIMP}}) \times T_{\text{eff}}^i$  (see Equation 4.2) is reported in Tables 5 and 6. Results for  $M_{\text{WIMP}} < 500$  GeV are available in Table 1.

Model	Parameter	Range
CMSSM	Common scalar mass	$50 \text{ GeV} < m_0 < 4 \text{ TeV}$
	Common gaugino mass	$500 \text{ GeV} < m_{1/2} < 2.5 \text{ TeV}$
	Ratio of vevs of the Higgs fields	$5 < \tan(\beta) < 62$
	Common trilinear coupling	$-5 \text{ TeV} < A_0 < 5 \text{ TeV}$
	Sign of the Higgs mixing	$\text{sgn}(\mu) > 0$
MSSM-7	Higgsino mass term	$-10 \text{ TeV} < \mu < 10 \text{ TeV}$
	Gaugino mass term	$-10 \text{ TeV} < M_2 < 10 \text{ TeV}$
	CP-odd Higgs boson mass	$60 \text{ GeV} < m_A < 1 \text{ TeV}$
	Trilinear couplings for	$-3m_0 < A_b < 3m_0$
	the third generation squarks	$-3m_0 < A_t < 3m_0$

**Table 3.** Range of parameters scanned for the CMSSM and MSSM-7 models.

Observable	Lower limit (95% CL)
$m_{\tilde{\chi}_1^\pm}$	$> 94 \text{ GeV}$
$m_{\tilde{g}}$	$> 500 \text{ GeV}$
$m_{\tilde{q}}$	$> 1100 \text{ GeV}$
$m_{\tilde{e}_L}$	$> 107 \text{ GeV}$
$m_{\tilde{e}_R}$	$> 73 \text{ GeV}$
$m_{\tilde{\mu}_{L,R}}$	$> 94 \text{ GeV}$
$m_{\tilde{\tau}_{L,R}}$	$> 81.9 \text{ GeV}$
$m_{\tilde{\nu}}$	$> 43.7 \text{ GeV}$
$m_{\tilde{\chi}_1^0}$	$> 46 \text{ GeV}$
$m_{\tilde{\chi}_2^0}$	$> 62.4 \text{ GeV}$
$m_{\tilde{\chi}_3^0}$	$> 99.9 \text{ GeV}$
$m_{\tilde{\chi}_4^0}$	$> 116 \text{ GeV}$
$m_{H^\pm}$	$> 79.3 \text{ GeV}$
$g^{\nu 1}$	$> 0.502$
Observable	Value
$M_h$	$125 \pm 2 \text{ GeV}$
$\delta a_\mu^{\text{SUSY}}$	$(28.7 \pm 16) \times 10^{-10}$
$\text{BR}(\bar{B} \rightarrow X_s \gamma)$	$(3.55 \pm 0.84) \times 10^{-4}$

**Table 4.** Summary of the observables used in the grid scan performed with the package DarkSUSY on the CMSSM and MSSM-7 free parameter space. **Top:** Observables for which only limits currently exist. The mass of the chargino  $\tilde{\chi}_1^\pm$ , gluino  $\tilde{g}$ , squarks  $\tilde{q}$ , sleptons  $\tilde{e}_L$ ,  $\tilde{e}_R$ ,  $\tilde{\mu}_{L,R}$  and  $\tilde{\tau}_{L,R}$ , sneutrinos  $\tilde{\nu}$ , neutralinos  $\tilde{\chi}_1^0$  (LSP and dark matter candidate in this analysis),  $\tilde{\chi}_2^0$ ,  $\tilde{\chi}_3^0$  and  $\tilde{\chi}_4^0$ , charged Higgs  $H^\pm$  and the effective neutrino coupling  $g^{\nu 1}$  from invisible Z-decay width [2]. **Bottom:** Observables for which a measurement is available. The Higgs boson  $h$  mass as an averaged result from CMS and ATLAS Collaborations [49], the discrepancy  $\delta a_\mu^{\text{SUSY}}$  between the experimental value and the SM prediction of the anomalous magnetic moment of the muon  $(g-2)_\mu$  [2] and the branching ratio of the b-hadron decay  $\bar{B} \rightarrow X_s \gamma$  [2].

$M_{\text{WIMP}}$ (GeV)	Channel	$\Psi_{\text{cut}}$ ( $^\circ$ )	$\mu^{90\%}$	$\bar{A}_{\text{eff}}(M_{\text{WIMP}})$ ( $\text{m}^2$ )	$\bar{\Phi}_{\nu_\mu+\bar{\nu}_\mu}$ ( $\text{km}^{-2}/\text{yr}$ )	$\Phi_{\nu_\mu+\bar{\nu}_\mu}$ ( $\text{km}^{-2}/\text{yr}$ )	$\Phi_\mu$ ( $\text{km}^{-2}/\text{yr}$ )	$\sigma_{\text{p,SD}}$ (pb)	$\sigma_{\text{p,SI}}$ (pb)
50	$b\bar{b}$	8.4	7.5	$6.9 \times 10^{-10}$	$7.5 \times 10^{15}$	$1.1 \times 10^{16}$	$2.4 \times 10^5$	$7.6 \times 10^{-1}$	$2.9 \times 10^{-3}$
	$\tau\bar{\tau}$	5.7	5.1	$8.2 \times 10^{-8}$	$5.0 \times 10^{13}$	$6.2 \times 10^{13}$	$1.1 \times 10^4$	$1.4 \times 10^{-3}$	$5.5 \times 10^{-6}$
80.3	$b\bar{b}$	5.7	5.1	$7.8 \times 10^{-9}$	$5.2 \times 10^{14}$	$6.6 \times 10^{14}$	$2.6 \times 10^4$	$1.0 \times 10^{-1}$	$2.7 \times 10^{-4}$
	$W^+W^-$	5.7	5.1	$4.2 \times 10^{-7}$	$9.7 \times 10^{12}$	$1.2 \times 10^{13}$	$6.0 \times 10^3$	$1.8 \times 10^{-3}$	$4.6 \times 10^{-6}$
	$\tau\bar{\tau}$	5.2	5.5	$6.3 \times 10^{-7}$	$6.1 \times 10^{12}$	$8.8 \times 10^{12}$	$3.9 \times 10^3$	$4.8 \times 10^{-4}$	$1.3 \times 10^{-6}$
100	$b\bar{b}$	5.7	5.1	$2.2 \times 10^{-8}$	$1.9 \times 10^{14}$	$2.4 \times 10^{14}$	$1.4 \times 10^4$	$5.5 \times 10^{-2}$	$1.2 \times 10^{-4}$
	$W^+W^-$	5.1	5.6	$1.4 \times 10^{-6}$	$2.7 \times 10^{12}$	$3.9 \times 10^{12}$	$3.1 \times 10^3$	$8.5 \times 10^{-4}$	$1.9 \times 10^{-6}$
	$\tau\bar{\tau}$	5.2	5.5	$1.3 \times 10^{-6}$	$2.9 \times 10^{12}$	$4.1 \times 10^{12}$	$2.9 \times 10^3$	$3.4 \times 10^{-4}$	$7.6 \times 10^{-7}$
150	$b\bar{b}$	5.2	5.5	$9.1 \times 10^{-8}$	$4.3 \times 10^{13}$	$6.1 \times 10^{13}$	$6.9 \times 10^3$	$3.1 \times 10^{-2}$	$5.1 \times 10^{-5}$
	$W^+W^-$	4.6	5.9	$5.1 \times 10^{-6}$	$7.0 \times 10^{11}$	$1.2 \times 10^{12}$	$2.0 \times 10^3$	$5.6 \times 10^{-4}$	$9.4 \times 10^{-7}$
	$\tau\bar{\tau}$	4.6	5.9	$4.0 \times 10^{-6}$	$9.0 \times 10^{11}$	$1.5 \times 10^{12}$	$2.1 \times 10^3$	$2.7 \times 10^{-4}$	$4.5 \times 10^{-7}$
176	$b\bar{b}$	5.2	5.5	$1.5 \times 10^{-7}$	$2.6 \times 10^{13}$	$3.8 \times 10^{13}$	$5.5 \times 10^3$	$2.5 \times 10^{-2}$	$3.8 \times 10^{-5}$
	$W^+W^-$	4.6	5.9	$7.8 \times 10^{-6}$	$4.6 \times 10^{11}$	$7.6 \times 10^{11}$	$1.8 \times 10^3$	$5.0 \times 10^{-4}$	$7.7 \times 10^{-7}$
	$\tau\bar{\tau}$	4.6	5.9	$6.0 \times 10^{-6}$	$6.0 \times 10^{11}$	$9.9 \times 10^{11}$	$1.9 \times 10^3$	$2.5 \times 10^{-4}$	$3.8 \times 10^{-7}$
200	$b\bar{b}$	5.2	5.5	$2.1 \times 10^{-7}$	$1.9 \times 10^{13}$	$2.7 \times 10^{13}$	$4.7 \times 10^3$	$2.3 \times 10^{-2}$	$3.2 \times 10^{-5}$
	$W^+W^-$	4.2	3.1	$9.7 \times 10^{-6}$	$3.5 \times 10^{11}$	$3.2 \times 10^{11}$	$8.9 \times 10^2$	$2.8 \times 10^{-4}$	$3.9 \times 10^{-7}$
	$\tau\bar{\tau}$	4.6	5.9	$8.0 \times 10^{-6}$	$4.5 \times 10^{11}$	$7.4 \times 10^{11}$	$1.7 \times 10^3$	$2.4 \times 10^{-4}$	$3.4 \times 10^{-7}$
250	$b\bar{b}$	5.2	5.5	$3.8 \times 10^{-7}$	$1.0 \times 10^{13}$	$1.5 \times 10^{13}$	$3.6 \times 10^3$	$1.9 \times 10^{-2}$	$2.4 \times 10^{-5}$
	$W^+W^-$	4.1	3.2	$1.4 \times 10^{-5}$	$2.4 \times 10^{11}$	$2.2 \times 10^{11}$	$8.5 \times 10^2$	$3.0 \times 10^{-4}$	$3.8 \times 10^{-7}$
	$\tau\bar{\tau}$	4.2	3.1	$1.2 \times 10^{-5}$	$2.9 \times 10^{11}$	$2.6 \times 10^{11}$	$8.4 \times 10^2$	$1.3 \times 10^{-4}$	$1.6 \times 10^{-7}$
350	$b\bar{b}$	5.2	5.5	$7.7 \times 10^{-7}$	$5.0 \times 10^{12}$	$7.1 \times 10^{12}$	$2.7 \times 10^3$	$1.8 \times 10^{-2}$	$1.9 \times 10^{-5}$
	$W^+W^-$	3.8	3.3	$2.4 \times 10^{-5}$	$1.4 \times 10^{11}$	$1.4 \times 10^{11}$	$8.0 \times 10^2$	$3.9 \times 10^{-4}$	$4.1 \times 10^{-7}$
	$\tau\bar{\tau}$	4.1	3.2	$2.1 \times 10^{-5}$	$1.6 \times 10^{11}$	$1.5 \times 10^{11}$	$7.7 \times 10^2$	$1.5 \times 10^{-4}$	$1.6 \times 10^{-7}$

**Table 5.** Results after optimisation and unblinding for the angular separation  $\Psi_{\text{cut}}$ , the 90% CL upper limit on the expected signal  $\mu^{90\%}$ , the total averaged effective area  $\bar{A}_{\text{eff}}(M_{\text{WIMP}}) = \sum_i \bar{A}_{\text{eff}}^i(M_{\text{WIMP}}) \times T_{\text{eff}}^i$  (with  $i$  corresponding to a given period of the detector), the 90% CL sensitivities on the neutrino+anti-neutrino flux at the Earth  $\bar{\Phi}_{\nu_\mu+\bar{\nu}_\mu}$ , and the 90% CL limits on the neutrino+anti-neutrino flux at the Earth  $\Phi_{\nu_\mu+\bar{\nu}_\mu}$ , on the muon flux at the detector  $\Phi_\mu$  ( $E_\mu > 1$  GeV), and on the spin-dependent and spin-independent WIMP-proton cross-sections  $\sigma_{\text{p,SD}}$  and  $\sigma_{\text{p,SI}}$  respectively. Results for  $M_{\text{WIMP}} > 350$  GeV are available in Table 6.

$M_{\text{WIMP}}$ (GeV)	Channel	$\Psi_{\text{cut}}$ ( $^\circ$ )	$\mu^{90\%}$	$\bar{A}_{\text{eff}}(M_{\text{WIMP}})$ ( $\text{m}^2$ )	$\bar{\Phi}_{\nu_\mu+\bar{\nu}_\mu}$ ( $\text{km}^{-2}/\text{yr}$ )	$\Phi_{\nu_\mu+\bar{\nu}_\mu}$ ( $\text{km}^{-2}/\text{yr}$ )	$\Phi_\mu$ ( $\text{km}^{-2}/\text{yr}$ )	$\sigma_{\text{p,SD}}$ (pb)	$\sigma_{\text{p,SI}}$ (pb)
500	$b\bar{b}$	4.6	5.9	$1.4 \times 10^{-6}$	$2.7 \times 10^{12}$	$4.4 \times 10^{12}$	$2.4 \times 10^3$	$2.2 \times 10^{-2}$	$2.0 \times 10^{-5}$
	$W^+W^-$	3.6	1.7	$3.5 \times 10^{-5}$	$9.1 \times 10^{10}$	$4.7 \times 10^{10}$	$3.8 \times 10^2$	$2.7 \times 10^{-4}$	$2.5 \times 10^{-7}$
	$\tau\bar{\tau}$	3.8	3.3	$3.4 \times 10^{-5}$	$9.7 \times 10^{10}$	$9.9 \times 10^{10}$	$7.6 \times 10^2$	$2.0 \times 10^{-4}$	$1.8 \times 10^{-7}$
750	$b\bar{b}$	4.6	5.9	$2.3 \times 10^{-6}$	$1.6 \times 10^{12}$	$2.6 \times 10^{12}$	$2.1 \times 10^3$	$2.9 \times 10^{-2}$	$2.4 \times 10^{-5}$
	$W^+W^-$	3.6	1.7	$4.6 \times 10^{-5}$	$6.9 \times 10^{10}$	$3.6 \times 10^{10}$	$3.7 \times 10^2$	$4.9 \times 10^{-4}$	$4.0 \times 10^{-7}$
	$\tau\bar{\tau}$	3.6	1.7	$4.8 \times 10^{-5}$	$6.7 \times 10^{10}$	$3.4 \times 10^{10}$	$3.7 \times 10^2$	$1.6 \times 10^{-4}$	$1.3 \times 10^{-7}$
1000	$b\bar{b}$	4.2	3.1	$3.1 \times 10^{-6}$	$1.1 \times 10^{12}$	$1.0 \times 10^{12}$	$1.0 \times 10^4$	$2.0 \times 10^{-2}$	$1.5 \times 10^{-5}$
	$W^+W^-$	3.2	1.8	$4.9 \times 10^{-5}$	$6.3 \times 10^{10}$	$3.5 \times 10^{10}$	$4.0 \times 10^2$	$8.9 \times 10^{-4}$	$6.9 \times 10^{-7}$
	$\tau\bar{\tau}$	3.6	1.7	$5.8 \times 10^{-5}$	$5.5 \times 10^{10}$	$2.9 \times 10^{10}$	$3.6 \times 10^2$	$2.3 \times 10^{-4}$	$1.8 \times 10^{-7}$
1500	$b\bar{b}$	4.1	3.2	$4.2 \times 10^{-6}$	$8.2 \times 10^{11}$	$7.7 \times 10^{11}$	$9.7 \times 10^3$	$3.4 \times 10^{-2}$	$2.5 \times 10^{-5}$
	$W^+W^-$	3.3	1.8	$4.9 \times 10^{-5}$	$6.3 \times 10^{10}$	$3.6 \times 10^{10}$	$4.4 \times 10^2$	$2.1 \times 10^{-3}$	$1.5 \times 10^{-6}$
	$\tau\bar{\tau}$	3.3	1.8	$6.0 \times 10^{-5}$	$5.1 \times 10^{10}$	$2.9 \times 10^{10}$	$4.1 \times 10^2$	$5.1 \times 10^{-4}$	$3.7 \times 10^{-7}$
2000	$b\bar{b}$	3.8	3.3	$4.8 \times 10^{-6}$	$6.8 \times 10^{11}$	$6.9 \times 10^{11}$	$9.9 \times 10^3$	$5.4 \times 10^{-2}$	$3.8 \times 10^{-5}$
	$W^+W^-$	3.3	1.8	$4.8 \times 10^{-5}$	$6.5 \times 10^{10}$	$3.7 \times 10^{10}$	$4.7 \times 10^2$	$3.9 \times 10^{-3}$	$2.8 \times 10^{-6}$
	$\tau\bar{\tau}$	3.3	1.8	$6.0 \times 10^{-5}$	$5.1 \times 10^{10}$	$2.9 \times 10^{10}$	$4.4 \times 10^2$	$9.1 \times 10^{-4}$	$6.4 \times 10^{-7}$
3000	$b\bar{b}$	3.8	3.3	$5.4 \times 10^{-6}$	$6.1 \times 10^{11}$	$6.2 \times 10^{11}$	$1.0 \times 10^3$	$1.1 \times 10^{-1}$	$7.3 \times 10^{-5}$
	$W^+W^-$	3.3	1.8	$4.3 \times 10^{-5}$	$7.2 \times 10^{10}$	$4.0 \times 10^{10}$	$5.3 \times 10^2$	$9.9 \times 10^{-3}$	$6.8 \times 10^{-6}$
	$\tau\bar{\tau}$	3.3	1.8	$5.5 \times 10^{-5}$	$5.6 \times 10^{10}$	$3.2 \times 10^{10}$	$5.0 \times 10^2$	$2.2 \times 10^{-3}$	$1.5 \times 10^{-6}$
5000	$b\bar{b}$	3.8	3.3	$6.1 \times 10^{-6}$	$5.4 \times 10^{11}$	$5.5 \times 10^{11}$	$1.0 \times 10^3$	$2.6 \times 10^{-1}$	$1.7 \times 10^{-4}$
	$W^+W^-$	3.6	1.7	$3.9 \times 10^{-5}$	$8.2 \times 10^{10}$	$4.3 \times 10^{10}$	$5.9 \times 10^2$	$3.0 \times 10^{-2}$	$2.0 \times 10^{-5}$
	$\tau\bar{\tau}$	3.6	1.7	$4.7 \times 10^{-5}$	$6.8 \times 10^{10}$	$3.5 \times 10^{10}$	$5.7 \times 10^2$	$6.7 \times 10^{-3}$	$4.5 \times 10^{-6}$
10000	$b\bar{b}$	3.8	3.3	$6.0 \times 10^{-6}$	$5.5 \times 10^{11}$	$5.6 \times 10^{11}$	$1.2 \times 10^3$	$1.0 \times 10^0$	$6.7 \times 10^{-4}$
	$W^+W^-$	3.3	1.8	$2.9 \times 10^{-5}$	$1.1 \times 10^{11}$	$6.0 \times 10^{10}$	$8.3 \times 10^2$	$1.7 \times 10^{-1}$	$1.1 \times 10^{-4}$
	$\tau\bar{\tau}$	3.3	1.8	$3.2 \times 10^{-5}$	$9.6 \times 10^{10}$	$5.4 \times 10^{10}$	$8.9 \times 10^2$	$4.1 \times 10^{-2}$	$2.7 \times 10^{-5}$

**Table 6.** Results after optimisation and unblinding for the angular separation  $\Psi_{\text{cut}}$ , the 90% CL upper limit on the expected signal  $\mu^{90\%}$ , the total averaged effective area  $\bar{A}_{\text{eff}}(M_{\text{WIMP}}) = \sum_i \bar{A}_{\text{eff}}^i(M_{\text{WIMP}}) \times T_{\text{eff}}^i$  (with  $i$  corresponding to a given period of the detector), the 90% CL sensitivities on the neutrino+anti-neutrino flux at the Earth  $\bar{\Phi}_{\nu_\mu+\bar{\nu}_\mu}$ , and the 90% CL limits on the neutrino+anti-neutrino flux at the Earth  $\Phi_{\nu_\mu+\bar{\nu}_\mu}$ , on the muon flux at the detector  $\Phi_\mu$  ( $E_\mu > 1$  GeV), and on the spin-dependent and spin-independent WIMP-proton cross-sections  $\sigma_{\text{p,SD}}$  and  $\sigma_{\text{p,SI}}$  respectively. Results for  $M_{\text{WIMP}} < 500$  GeV are available in Table 5.